Machine Learning-Enabled Direct Ink Writing of Conductive Polymer Composites for Enhanced Performance in Thermal Management and Current Protection

Abstract:
This study introduces a novel approach that leverages the synergy of machine learning (ML) and Direct Ink Writing (DIW) to optimize the manufacturing feasibility of conductive polymer composites (CPCs) films. The main research focus centers on precisely fine-tuning the printing parameters to strike the perfect balance between the high loading of dendritic copper fillers and their influences on processing and composite performance properties. This pioneering combination significantly enhances the precision of the final product without resorting to time-consuming procedures. ML algorithms contributed to identifying optimal printing variables such as speed, flow pressure, and filler concentration, which helped in identifying the optimal filler content and its performance capabilities. The resulting films exhibited thermo-resistive behavior with a noticeable resistivity increase by 6-7 orders of magnitude at elevated temperatures, specifically around 100°C. Furthermore, the study highlights remarkable strain-sensing capabilities, simultaneously showcasing a substantial increase in composite modulus. These discoveries bear substantial significance for the development of exceptionally functional thermal interface materials suitable for use in sensors, current collectors, and energy storage devices. The method presented here offers a promising pathway for advancing the fabrication and performance optimization of conductive polymer composites, opening up diverse applications in emerging technologies.

Keywords: Conductive polymer composites, direct ink writing, machine learning, thermal management

1. Introduction

Conductive polymer composites (CPCs) have attracted significant attention due to their versatile functional properties [1–3]. One common characteristic of CPCs is their ability to transition between insulating and conducting states by altering their resistivity with temperature [4–6]. Typically, these composites exhibit a noticeable increase in resistivity as the temperature rises, particularly around the melting temperature (T_m) of the crystalline polymer, a phenomenon known as the Positive-Temperature-Coefficient (PTC) effect [7–9]. The establishment of conductive pathways, referred to as the percolation threshold (P_c), plays a crucial role in these transitions and depends on the critical concentration of conductive filler. By carefully selecting polymer matrices and conductive additives, it is possible to achieve desirable mechanical, electrical, and thermal properties, making CPC suitable for various applications including thermal interface materials, self-regulated heaters, and over-current protectors, in portable electronic devices and battery applications [9–11]. The PTC behavior of composites can also be tailored by incorporating multiple polymers into the composite, creating a mixed polymer system [12]. Numerous studies have explored conductive semicrystalline composites by introducing materials such as carbon nanotubes (CNTs) [13] or carbon black (CB) [14]. For example, Pour et al. [8] investigated a binary polymer composite consisting of PMMA and LDPE with CB as the conductive filler. Yang et al. [15,16] studied an HDPE/PVDF/CNF polymer composite, observing a two-step PTC behavior with favorable reproducibility. Additionally, Wei et al. [17] found that incorporating UHMWPE as a second polymer in a CB/PP composite eliminated the Negative-Temperature-Coefficient (NTC) effect.

Enhancing the intensity of the PTC effect can be achieved through two main approaches: reducing resistivity at room temperature and increasing resistivity near the polymer melt temperature [18]. These objectives necessitate the optimization of filler concentration and a deeper understanding of the interparticle distances among the conductive particles within the composite. Unfortunately, conventional techniques like melt mixing often face limitations related to their rheological properties, making it challenging to achieve the desired outcomes. In contrast, 3D printing offers a departure from traditional methods, enabling the creation of intricate and tailored structures while facilitating optimized parametric studies tailored to specific applications or performance criteria [19]. Direct Ink Writing (DIW), an extrusion-based 3D printing technique widely utilized in this domain [20,21], further enhances versatility by allowing for the fine-tuning of ink properties, precise deposition control, and printing parameters. This results in improved geometries and enhanced performance characteristics [22].

DIW, as a rapid prototyping technique, faces a fundamental challenge in transitioning away from conventional trial-and-error methodologies towards more efficient quality control during manufacturing. The traditional approach to 3D printing often involves multiple iterations, adjustments, and recalibrations of printing parameters, leading to increased lead times and resource consumption. In this context, the role of machine learning (ML) becomes paramount [23]. ML-based data analysis, particularly when integrated with imaging analysis, offers a promising solution to expedite the process and predict optimal parameter designs [24,25]. Machine learning algorithms can harness the power of vast datasets generated during experiments, learning patterns and correlations that might not be immediately apparent to human operators [26]. By analyzing these data, ML models can identify trends, optimize printing parameters, and predict the ideal conditions for producing highly accurate results by meeting the user requirements. This capability not only reduces the need for extensive trial-and-error but also enhances manufacturing precision and efficiency. Furthermore, ML can provide real-time monitoring and control during the printing process, detecting potential issues and making immediate adjustments to ensure the final product meets the desired specifications [27,28]. This proactive approach minimizes the risk of defects, reduces material waste, and accelerates the overall production timeline.

In this study, we have introduced the K-Nearest Neighbors (KNN) model, which is a non-parametric supervised ML method with DIW to create opportunities for manufacturing conductive polymer nanocomposites with enhanced performance while eliminating the need for trial-and-error processes. DIW

typically operates with individual material extrusions, necessitating constant adjustments to printing parameters, including injection rates, travel speed, and drying kinetics [29,30]. To streamline this, the ML method automates decision-making for printing parameters, simplifying the search for optimal values. In this study, we introduce the incorporation of dendritic copper (Cu) into a binary polymer blend, with polyvinyl difluoride (PVDF) chosen as the rich phase due to its high thermal expansion coefficient. While DIW offers precise control over depositing Cu particles in a patterned manner, ML optimization enhances the loading of conductive fillers and improves the understanding of their connectivity arrangements, ultimately enhancing the PTC behavior with accompanied electrical and mechanical performance. This novel approach aims to unravel how dendritic fillers' unique characteristics influence their alignment, conductivity, and the overall performance of the composite material.

2. Experimental

2.1 Materials

Copper-powder (dendritic, <45 μm, 99.7% trace metals basis, Sigma Aldrich), Polyvinyl difluoride (PVDF) (Mw: 477,000 g/mol), polyethylene glycol (PEG) 20,000 (Mw: 20,000 g/mol, Sigma-Aldrich), Dimethylformamide (DMF) (Anhydrous, >99.5%, CAS #67-68-5) solvent was purchased from Sigma–Aldrich.

2.2 Preparation of Conducive Polymer Composite Feedstock

The fabrication of CPCs followed a systematic procedure. Initially, PVDF and PEG were blended in varying ratios, specifically PVDF: PEG ratios of 10:10, 15:8, and 20:6, as detailed in **Table 1**. For instance, in the case of the PVDF20/PEG06 mixture, 1g of PVDF and 0.3g of PEG were combined and dissolved in 5 ml of DMF. This dissolution process involved a combination of sonication and magnetic stirring at a temperature of 40°C. Sonication was carried out for 10 minutes, followed by 4 hours of magnetic stirring to ensure thorough blending. The chosen time intervals were designed to facilitate effective mixing while preventing excessive heating of the solution.

To enhance the electrical conductivity of the material for battery applications, spiky copper particles were introduced into the polymer solution containing PEG/PVDF/DMF. Different concentrations of dendritic Cu particles were uniformly incorporated into the viscous polymer solution, as detailed in **Figure 1** and **Table 1**. For instance, varying amounts of Cu, ranging from 0.1 to 1 gram, were introduced into the solutions containing 1g of PVDF, 0.3g of PEG, and 5ml of DMF, and the mixtures were subjected to speed mixing around 200 rpm for 2 minutes until a homogeneous colloid was achieved. This dispersion process was carefully executed through a combination of stirring and high-speed mixing to ensure well-dispersed Cu particles without the risk of thermal degradation or particle agglomeration within the matrix. The meticulous dispersion of copper within the polymer matrix was a critical step to ensure uniform distribution.

2.3 Direct ink writing (DIW)

The inks were loaded into 10ml syringes and mounted onto a custom 3D-printed holder. This holder was connected to one of the printhead rails inside the 3D printer (System 30 M, from Hyrel 3D), enabling the setup to follow the imported G-code and achieve manufacturing autonomy. The choice of nozzle type with an 18-gauge nozzle diameter tip (equivalent to a 1.2 mm needle diameter) was crucial for ensuring the printability of various copper-loaded inks. This specific nozzle type provided precise control over ink flow and deposition. To maintain a continuous and uninterrupted ink flow, preventing clogging, we employed a pneumatic fluid dispenser, the Metcal DX-255. This pressure delivery system played a pivotal role in preserving deposition precision, preventing metal particle agglomeration, and ensuring the integrity of the resulting films.

We systematically adjusted the printing pressures and printing speeds, subsequently printing the inks as films onto glass substrates. The films were allowed to dry in an argon atmosphere for a duration of 5 to 8 hours to facilitate solvent evaporation. This meticulous process led to the creation of freestanding films,

each characterized by distinct polymer combinations, specifically PVDF/PEG, at varying ratios of copper particles. The printing pressure, measured in pounds per square inch (PSI), was a critical factor as it influenced the ink flow rate and, consequently, the rate of copper deposition. By employing the DIW approach, we benefit from the flexibility to adjust printing height and execute prints with one or more layers. However, our study specifically concentrated on single-layer printing with a layer height of 0.1 mm. Moreover, our attention towards fine-tuning printing pressure and speeds was essential for achieving the desired copper loading and optimizing the printability characteristics of the films.

2.4 Characterization

Differential scanning calorimetry (DSC) analyses were conducted utilizing the TA Instrument Q20 under a nitrogen atmosphere. These tests aimed to ascertain a range of phase change temperatures, including the melt temperature (T_m), and crystallization temperature (T_c). In our study, the baseline in DSC experiments is established using an empty pan or an inert reference material. Defining the baseline as zero allowed for the isolation and quantification of the heat flow associated specifically with sample transitions or reactions. Further, the samples were initially equilibrated to a temperature of 30°C and subsequently subjected to a heating cycle from 30°C to 200°C at a rate of 10°C per minute. The same cooling rate was applied to return to the initial temperature of 30°C.

The rheological properties of solutions containing PEG/PVDF/DMF with varying Cu concentrations were investigated using a 25 mm parallel plate rheometer equipped with a Peltier plate (Discover hybrid rheometer HR2, TA Instruments). The viscoelastic characteristics of the PEG/PVDF polymer blend solution with different Cu concentrations were examined at room temperature (approximately 23°C). Viscosity measurements were conducted over a shear rate range of 0.01 to 1000 s^{-1}, while storage and loss moduli were determined across an angular frequency range of 0.1 to 100 rad s^{-1}.

Scanning Electron Microscopy (SEM) (i.e., SEM/Focused Ion Beam (FIB), Auriga (Zeiss)) at an operating voltage of 5 kV, examinations were conducted on the 3D-printed samples to assess the influence of Cu concentration on dispersion quality. Additionally, optical imaging was performed using a confocal microscope to visualize the copper connectivity of various printing parameters.

A comprehensive analysis of the electrical conductivity and resistivity behaviors of the composite materials was conducted. Initially, we examined the room temperature electrical conductivity measurements using the 4-probe method, employing a digital multimeter connected to four probes strategically positioned on a sample with dimensions of 20mm in length. Subsequently, we conducted thermo-electrical investigations to evaluate the thermal response characteristics of these composite films under extreme thermal conditions. For these experiments, the composite films were connected to copper wires at both ends and attached to a thermocouple wire and the PTC effect of various composites was tested using the two-terminal method by ramping the temperature range from 30°C to 120°C within a heating furnace. The corresponding changes in resistance using a Keithley Multimeter 4200 were recorded and monitored as a function of the temperature variations using a digital multimeter. Additionally, the resistance measurements as a function of strain were conducted to assess the strain-sensing capabilities and mechanical durability of the composites using a Discover hybrid rheometer HR2 from TA Instruments.

Moreover, stress-strain testing was conducted at strain rates consistent with the resistance measurements using a tensile tester (Discover hybrid rheometer HR2, TA Instruments). The dry solid films were cut into sections, each measuring 20 mm in length and 10 mm in width, with an approximate thickness of 0.08 mm for each sample. These samples were then subjected to a tension rate of 5 mm/min for a duration of 500 seconds. The resulting stress-strain curves provided valuable data about the modulus of the composite films and their strength and strain characteristics at specific resistivity values.

3. Results and Discussions

Our research integrates 3D printing with machine learning to streamline the fabrication of conductive polymer composites and enhance their performance characteristics. **Figures 1a-1c** provide a comprehensive overview of the step-by-step procedure involved in the preparation and 3D printing of the samples. Initially, the PVDF/PEG blend is dispersed with a suitable solvent (i.e., DMF), as shown in **Figure 1a$_1$**. Subsequently, **Figure 1a$_2$-a$_3$** highlights the structural characteristics of the conductive filler incorporated within the polymer blend. The films are then meticulously fabricated through DIW, depicted in **Figure 1b**, allowing precise control over the deposition and solid loading by manipulating various printing parameters to enhance the film's conductivity properties. **Figure 1b$_1$** illustrates the polymer chains connecting the filler particles, with their connectivity being modulated through adjustments in inter-particle distance via different printing parameters, as demonstrated in **Figure 1b$_2$**.

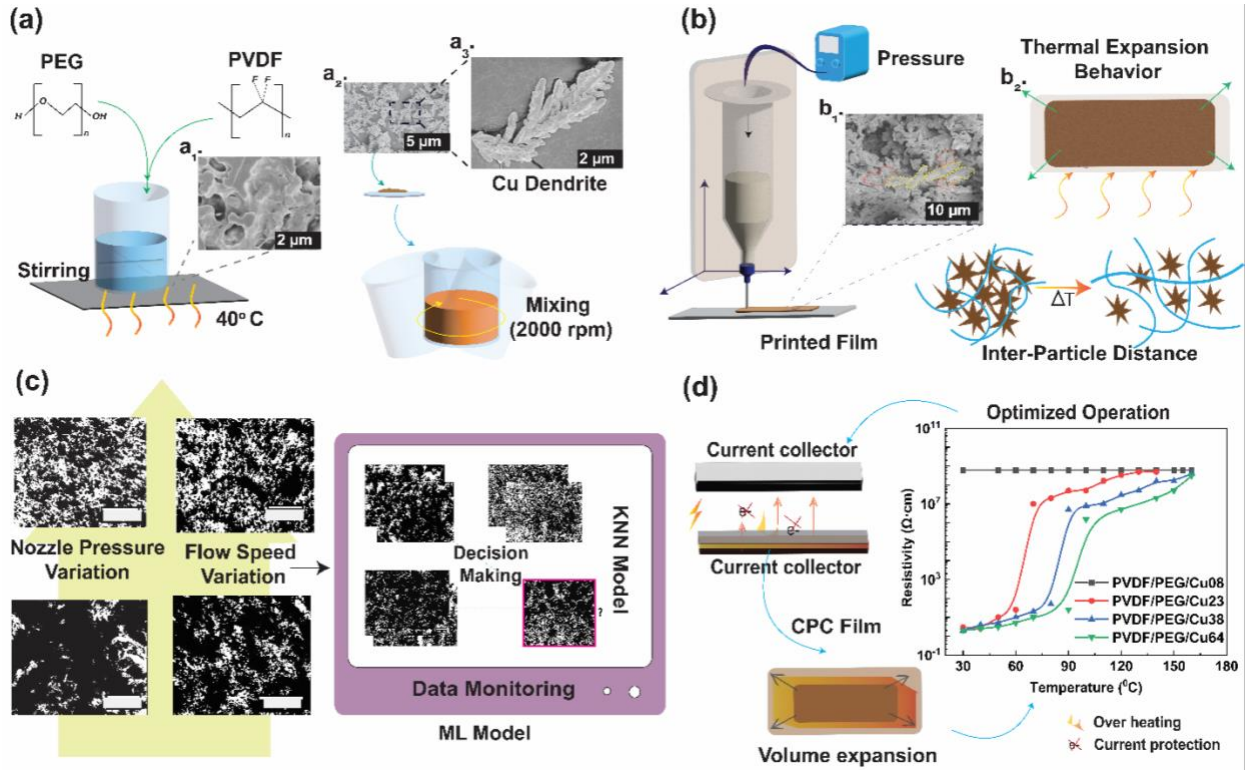

Figure 1. a) A schematic representation of the process for preparing PVDF/PEG blend as feedstock for 3D printing via magnetic stirring, accompanied by a$_1$) a scanning electron microscopy (SEM) image displaying PVDF/PEG film post drying (a scale bar of 2 µm) with (a$_2$-a$_3$) zoomed-in SEM image highlighting the dendritic Cu particle structure (a scale bar of 5 and 2 µm in a$_2$-a$_3$, respectively). b) A schematic illustration of the direct ink writing (DIW) setup using a pneumatic dispenser to produce composite films maintaining b$_1$) interfacial contact between the polymer and Cu particles (scale bar - 10 µm), along with the capability of having b$_2$) thermal expansion behavior of the film and interparticle distance among dendritic Cu fillers. c) An Illustration showing the variations in filler distribution with changes in 3D printing parameters, such as flow pressure and injection speed, further highlights the application of AI/ML-based data analytics for the imaging analysis of printed samples. d) A schematic illustration emphasizing the potential application in thermal management and current protection highlighting its energy storage performance characteristics.

While traditional techniques often involve melting for film preparation, leading to loose network conductive fillers due to an excess of polymer, our approach capitalizes on 3D printing's versatility in creating customized structures tailored to specific applications or performance criteria [21]. Nevertheless, navigating the multitude of 3D printing parameters can often entail extensive trial-and-error studies,

potentially consuming valuable time. To mitigate this, our research introduces ML to train models through parametric studies, achieving predictions with 100% accuracy matching our experimental measurements, as illustrated in **Figure 1c**. These ML-guided predictions and model training methods have enabled us to fabricate films with exceptional performance characteristics, as highlighted in **Figure 1d**. This breakthrough not only eliminates time-consuming studies but also positions these films for potential applications in thermosensitive sensors, over-current protectors, and thermal interface materials for battery applications. In summary, our research bridges the gap between 3D printing and machine learning, offering an efficient and precise approach to optimize CPC fabrication. In addition, the integration of machine learning into our 3D printing marks a transformative shift towards more intelligent and data-driven manufacturing processes. It empowers manufacturers to streamline their operations, achieve higher levels of automation, and deliver superior-quality products in a shorter timeframe, ultimately revolutionizing the way we approach additive manufacturing.

3.1 Material Selection and Composition Rationale

CPCs have attracted significant interest in battery technology due to their unique properties, which include good electrical conductivity, mechanical flexibility, and chemical stability [31–33]. These materials can be used in various components of batteries, enhancing their performance, longevity, and safety. Some of the key applications and benefits of CPCs in battery technology include electrodes, electrode additives, separator coatings, and interfacial layers [34,35]. While the application of CPCs in commercial battery systems for thermal management purposes may not be extensively documented, however, there is literature highlighting scientific research merits based on its fundamental science that can be utilized in enhancing thermal safety and performance as shown in **Table S1**. When the temperature rises, causing an increase in resistivity, the composite can limit the flow of electrical current, effectively reducing the heat generated within the system, this can be applied to any energy storage devices. This passive thermal regulation can help maintain the heated device temperature within safe operating limits. Effective thermal response in polymers requires a qualified polymer matrix that meets specific criteria: a large thermal expansion coefficient (α), a suitable T_m, compatibility during operation, and wide availability at a low cost [36]. After evaluating some candidates (such as those in **Table S2**), PEG and PVDF were chosen due to their optimal properties in fulfilling these criteria.

The initial focus of the study was on polymer blends without metal additives, specifically examining their composition effects on printability and phase transition characteristics. A range of PVDF and PEG combinations were investigated to identify the ideal polymer concentration for formulating the feedstock blend. Within the polymer blend, the rich phase was selected as PVDF, due to its high thermal expansion coefficient that may prevent overheating [15]. Various ratios of PVDF and PEG were mixed and assessed for their processability (as shown in **Table 1**). The transition temperatures observed in the polymer mixtures closely mirrored those of the individual PVDF and PEG components, as depicted in **Figure 1** and detailed in **Table 1**. For instance, PVDF20/PEG06 exhibited melting points (T_m) of approximately 60°C and 173°C, closely matching the individual PVDF (around 63°C) and PEG (approximately 174°C) values. This composition was deemed optimal due to its homogeneous blend behavior (**Figure 1a$_1$**), favorable printability, and compatibility with Cu fillers (**Table 1**). Higher PEG concentrations, such as PVDF15/PEG8 and PVDF10/PEG10, were avoided due to their rapid solidification in an open atmosphere, and phase separation was observed upon storing the solution for less than 24 hours, which led to printhead clogging issues **(Figure S1).** In conclusion, the PVDF20/PEG06 blend emerged as the most suitable composition for further experimentation in this project.

Table 1. Correlation of polymer concentrations with processing parameters

Type	Terminology	Composition (wt.%) in solutions			Cu in solid samples	Processability		Thermal Properties from DSC					
		PVDF/ Solvent (wt%)	PEG/ Solvent (wt%)	Cu/ solvent (wt%)	Cu/ polymer (wt%)	Printability	Miscibility of blend with Cu of different concentrations	T_m for PEG/PVDF (°C)	T_c for PEG/PVDF (°C)	ΔH_f for PVDF (J/g)	ΔH_f for PEG (J/g)	$X_{c\text{-}PVDF}$ (%) for PVDF	$X_{c\text{-}PEG}$ (%) for PEG
Pure	PVDF	20	N/A	0	0	Yes	*N/A*	*173.05*	*137.10*	*5.75*	*N/A*	*24.26*	*N/A*
	PEG	*N/A*	*40*			Yes	*N/A*	67.23	*45.34*	*N/A*	*40.12*	*N/A*	*53.01*
Blends	PVDF10/PEG10	10	10			*No*	*No*	*N/A*	*N/A*	*N/A*	*N/A*	*N/A*	*N/A*
	PVDF15/PEG08	15	8			*No*	*No*	*N/A*	*N/A*	*N/A*	*N/A*	*N/A*	*N/A*
	PVDF20/PEG06	*20*	*6*			*Yes*	*Yes*	*63.42 & 174.13*	*47.21 & 143.33*	*5.80*	*9.49*	*27.74*	*83.74*
Composite inks for 3D printing	*PVDF/PEG/Cu08*	*20*	*6*	*2*	*8*	*Yes*	*Yes*	*63.31 & 174.10*	*46.32 &144.54*	*7.50*	*4.99*	*35.86*	*44.08*
	PVDF/PEG/Cu23			*6*	*23*			*62.50 & 173.33*	*46.10 &145.29*	*8.05*	*4.11*	*38.49*	*36.29*
	PVDF/PEG/Cu38			*10*	*38*			*57.47 & 173.55*	*44.53 &146.67*	*10.29*	*3.61*	*49.23*	*31.86*
	PVDF/PEG/Cu54			*14*	*54*			*58.49 & 173.46*	*45.62 & 146.43*	*11.60*	*2.20*	*55.45*	*19.47*
	PVDF/PEG/Cu62			*16*	*62*	*No*	*No*	*N/A*	*N/A*	*N/A*	*N/A*	*N/A*	*N/A*

Note: T_m, melting temperature from the heating stage; T_c, crystallization temperature from the cooling stage; X_c, crystallization degree

Copper fillers were incorporated into the polymer blends to enhance electrical conductivity for battery applications [37]. The dendritic structure of copper, as utilized in this project, plays a crucial role as it enhances charge transport through tunneling effects owing to its increased surface area compared to other shapes like spheres and flakes [38]. The inclusion of our Cu dendritic metallic fillers offers a dual benefit – it not only lowers the filler concentration thanks to the network structure but also enhances electrical performance due to its high conductivity and aspect ratio. **Figures 1a$_2$-1a$_3$** display SEM images of these dendritic copper particles, which effectively occupy available space within the polymer blends, facilitating the formation of conductive networks. Furthermore, the use of a binary polymer matrix strategy, employing a PVDF/PEG blend, contributes to improving composite consistency by constraining filler movement [39]. within the "rich" PVDF phase, allowing for the development of conductive networks with dendritic copper particles at the interface of the polymer blend and within the rich phase. This selected blend consists of polymers with high and low thermal expansion coefficients, enabling selective dispersion within one phase and tunable percolation concerning film operating temperatures compared to a single semi-crystalline phase. Additionally, PEG functions as a plasticizer, aiding in the dispersion of conductive fillers [40].

Moreover, DSC experiments were conducted to assess the compatibility of different polymer compositions. This included pure polymer compositions and blends of PEG/PVDF containing Cu conductive fillers. The peaks of the T_c and T_m for the pure PVDF and PEG are shown in **Figures S2 & S3**, which were also summarized in **Table 1**. For the blend polymer blends, **Figures 2a-b** illustrate the results of these experiments. The introduction of Cu into the blend had a minor impact on the T_m of PVDF, with a slight decrease observed in PVDF/PEG/Cu54 compared to PVDF/PEG. Namely, the T_m of PVDF showed relatively little change (i.e., 1 °C decrease from 174.13 to 173.46 °C in composites as compared to the pure blend, **Figure 2a**). More interesting, the addition of Cu to the PVDF/PEG blend has increased both the crystallization temperature (i.e., T_c from 143.33 °C to 146.67 °C) and crystallinity (i.e., *X_c from 27.74% to 55.45%*) of PVDF. However, with a further increase in Cu content, the T_m of PEG decreased from approximately 63.42 °C from PVDF/PEG blends to 58.49 °C in PVDF/PEG/Cu54, coinciding with a reduction in the crystallization temperature (i.e., T_c from 47.21 °C to 45.62 °C) and composite crystallinity (i.e., *X_c from 83.74% to 19.47%*). See the calculation of crystallinity degree in **SI**. It's worth noting that T_m reflects the crystalline phase, while T_g, representing the glass transition, is associated with the amorphous phase.

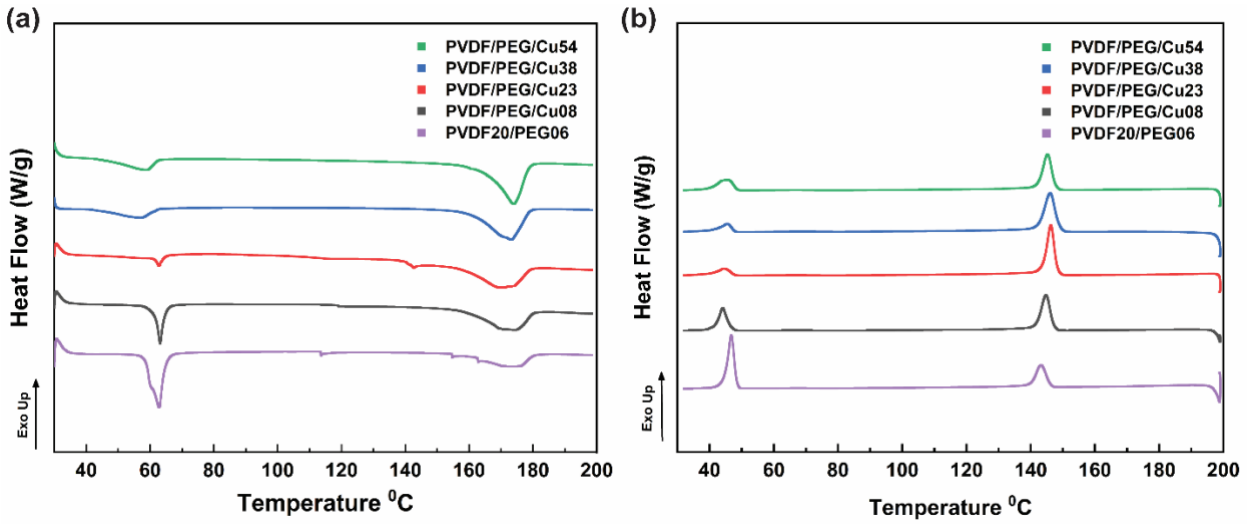

Figure 2. Differential Scanning Calorimetry (DSC) curves depicting the behavior of PVDF/PEG/Cu-based composite with varying Cu filler concentrations (namely, PVDF/PEG/Cu08, PVDF/PEG/Cu23, PVDF/PEG/Cu38, PVDF/PEG/Cu54) are shown for both the a) heating cycle, revealing melting peaks, and b) cooling cycle, displaying crystallization peaks.

The positive temperature coefficient (PTC) effect in most polymer composites typically occurs around one of these phase transition temperatures due to the polymer's volume change disrupting the conductive filler network. Adjusting the melting temperature via rational blending ratios can enable the films to function effectively at lower temperatures. As indicated in **Table 1**, the crystallinity of PVDF on its own within the PVDF20/PEG06 polymer blend is relatively low, approximately 27.74%. However, the introduction of copper filler has significantly raised the crystallinity to about 55.45% for PVDF20/PEG06/Cu54. This enhancement can be attributed to copper's role as a nucleation agent for PVDF crystallization. Copper effectively aids in aligning polymer chains, facilitating their mobility and ultimately resulting in increased crystallinity. Conversely, this trend differs for PEG due to its inherently less ordered structure [41]. In the presence of copper, low-concentrated PEG chains experience reduced mobility, limiting their ability to crystallize efficiently. This observation aligns with the obtained data, which demonstrates a decrease in PEG crystallinity from 83.74% to 19.47% with increasing Cu content.

3.2 Manufacturing Feasibility

3.2.1 3D Printing Feasibility

The decision to employ 3D printing as our primary film development method stemmed from its numerous advantages over conventional coating techniques. DIW in 3D printing facilitates rapid prototyping, allowing for quick and cost-effective iterations of film designs. This is particularly advantageous in research and development phases where experimentation and testing are essential. This is advantageous in scenarios were producing films in small quantities or as needed is more practical and cost-effective [42,43]. To assess the printability of the ink, we conducted a study on the rheological properties of the polymer blend and PVDF/PEG-Cu conductive composite inks, as depicted in **Figure 3a**. All inks exhibited a shear-thinning behavior, a crucial rheological characteristic for DIW. At low shear rates, the ink exhibits a notably high viscosity, which gradually decreases with increasing shear rate (**Figure 3a**).

In our pursuit of assessing structural stability, we systematically explored the effects of copper concentration on storage/loss moduli in composite inks, as shown in **Figures 3b-3c**, where the storage modulus (G') begins to rise after a specific threshold for each sample. Both the filler fraction and the deformation state of the elementary chain within the network significantly influence this behavior. In the case of a viscoelastic solid, G' remains constant and predominates at low frequencies, while loss modulus (G") increases with higher frequencies, taking precedence at the upper end of the spectrum. G' possesses a value roughly an order of magnitude higher than G", consistent with the ink displaying elastic solid behavior. This behavior is indicative of the strong physical interactions (such as van der Waals forces) between the particles and the polymer, which effectively uphold the entire gel network, resulting in a self-supporting ink. It is also observed that the storage modulus and viscosity of the polymer blend decrease with an increase in copper concentrations. This is due to the dispersion and distribution of Cu in the solution that may facilitate the macromolecular flow during shearing. For instance, from **Figure 3b**, the modulus has decreased from ~10^{-3} MPa in polymer blends to ~10^{-5} MPa in composite inks at an angular frequency of 0.1 rad/s, which is approximately 2 orders of decrease in magnitude.

However, an increase in G' corresponds to clogging tendencies at very high printing speeds and is proportional to the ink's storage duration. These issues can be mitigated by reducing the polymer weight percentage while keeping the optimum copper percentages. For instance, higher copper concentrations of more than 60 wt% can affect the printing, leading to unevenly structured films **(Figure S4)**, this is because copper will start to settle and disrupt the shape of the print with excess Cu content. As a result, we fine-tuned the polymer concentrations to a broader range, opting for a PVDF20/PEG06, to strike the optimal balance between viscosity behavior and printability. Further, by maintaining proper solution mixing conditions before printing we have incorporated copper particles into the polymer matrix through DIW ensuring the even distribution of these conductive fillers, affording precise control over the deposition process (**Figure 3d**). As illustrated in **Figures 3d$_1$-d$_2$**, we have successfully printed a freestanding film composed of PVDF/PEG/Cu54. The film's flexibility without any cracks is attributed to our ability to

regulate copper deposition. In addition to this, **Figures 3d$_3$-d$_4$** show the SEM images of both the surface and cross-sectional distribution of copper in the matrix. Typically, the mechanical strength and flexibility of a film containing dense copper materials are compromised. However, this technique allows us to maintain both the film's thickness and uniformity, enabling us to customize the copper content and blend consistency, as compared to conventional methods. For our prints, we opted for a single-layer approach, adjusting our printing parameters—speeds and pressures—to increase copper content while maintaining even distribution within the film. Thus, in our study, we printed at a layer height of approximately 0.1 mm, followed by a drying process. The resulting film thickness, measured using a screw gauge, was approximately 80 µm. Moreover, the fabricated film shows synergistic behaviour towards their mechanical properties which decreases difficulties when applied to user-required applications This technical subtlety plays a crucial role in the development of highly flexible films with excellent conductivity properties, all while utilizing a high-volume fraction of Cu particles through extrusion-based 3D printing technology.

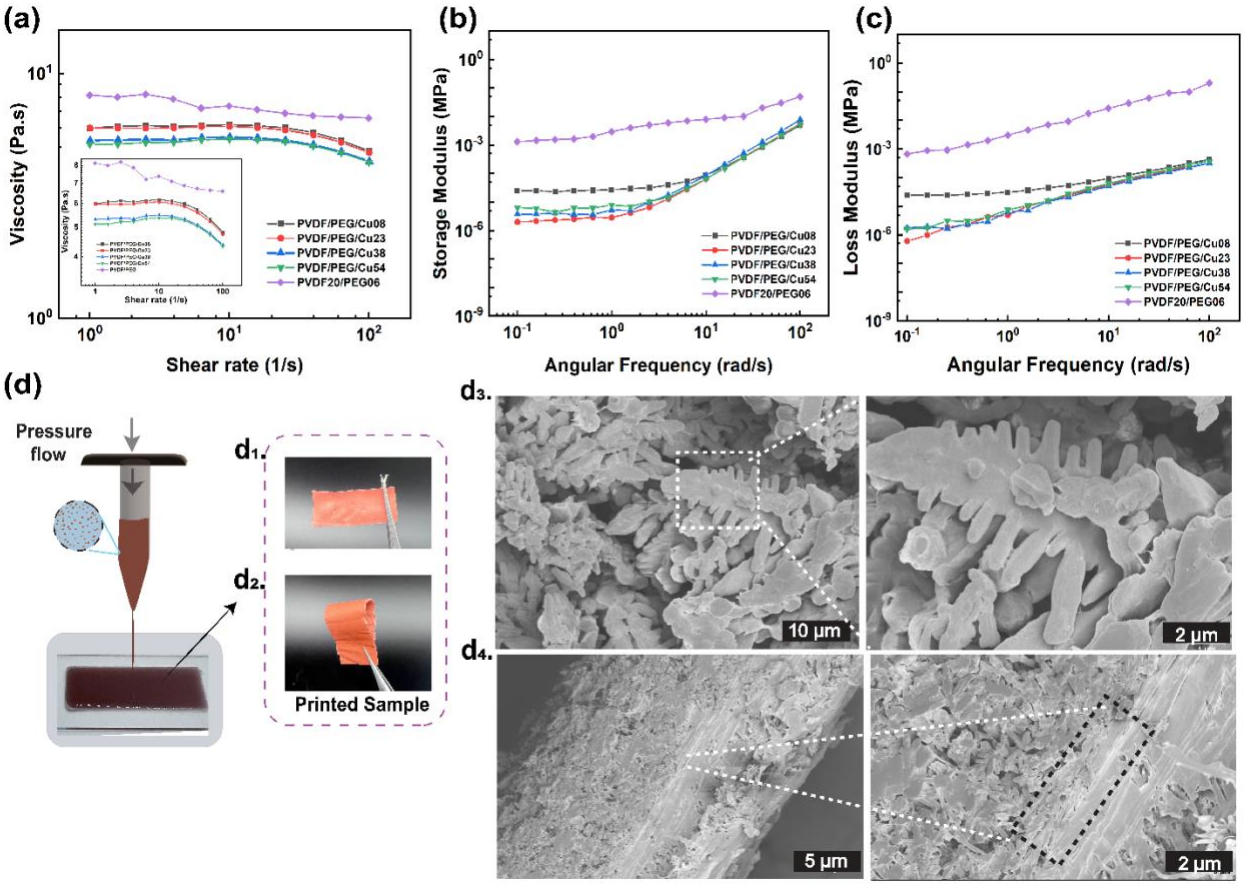

Figure 3. The rheological characteristics of PVDF/PEG/Cu inks with varying Cu concentrations (specifically, ~0, 8, 23, 38, and 54wt% in polymers) are presented, highlighting: a) viscosity vs. shear rate (10-1000 rad/s) along with the b) storage modulus vs. angular frequency and c) the loss modulus vs. angular frequency. Additionally, the d) 3D printed PVDF/PEG/Cu38 samples are showcased as one example, accompanied by optical images depicting d_1) the surface and d_2) a bent sample that demonstrates the film's flexibility without fracturing. The figure also includes SEM images illustrating the d_3) surface and d_4) cross-section of the printed samples.

3.2.2 *Rapid Prototyping Capability from DIW*

The impact of the printing parameters explored in this investigation offers a promising solution for controlling the deposition of fillers with excellent electrical conductivity, with potential applications in

over-current protection and thermal interface materials. To understand the alterations in filler connectivity or deposition quantity during printing, it was crucial to gain a comprehensive understanding of the parametric effects, as depicted in **Figure 4**. To assess the quality of Cu distribution, our original confocal microscope images were adjusted to the RGB color threshold without altering the figure's authenticity, revealing filler connections (**Figure S5**). Throughout the 3D printing process, the nozzle size and the distance between the nozzle tip and the substrate remained consistent across all prints (**Table S2**). Specifically, this study delved into the interaction between nozzle speed and flow pressure. The versatility explored herein focused on parametric variations, with PVDF/PEG/Cu23 serving as an illustrative example. These controlled parameter variations allowed us to analyze copper particle connectivity, such as interparticle distances, under diverse conditions.

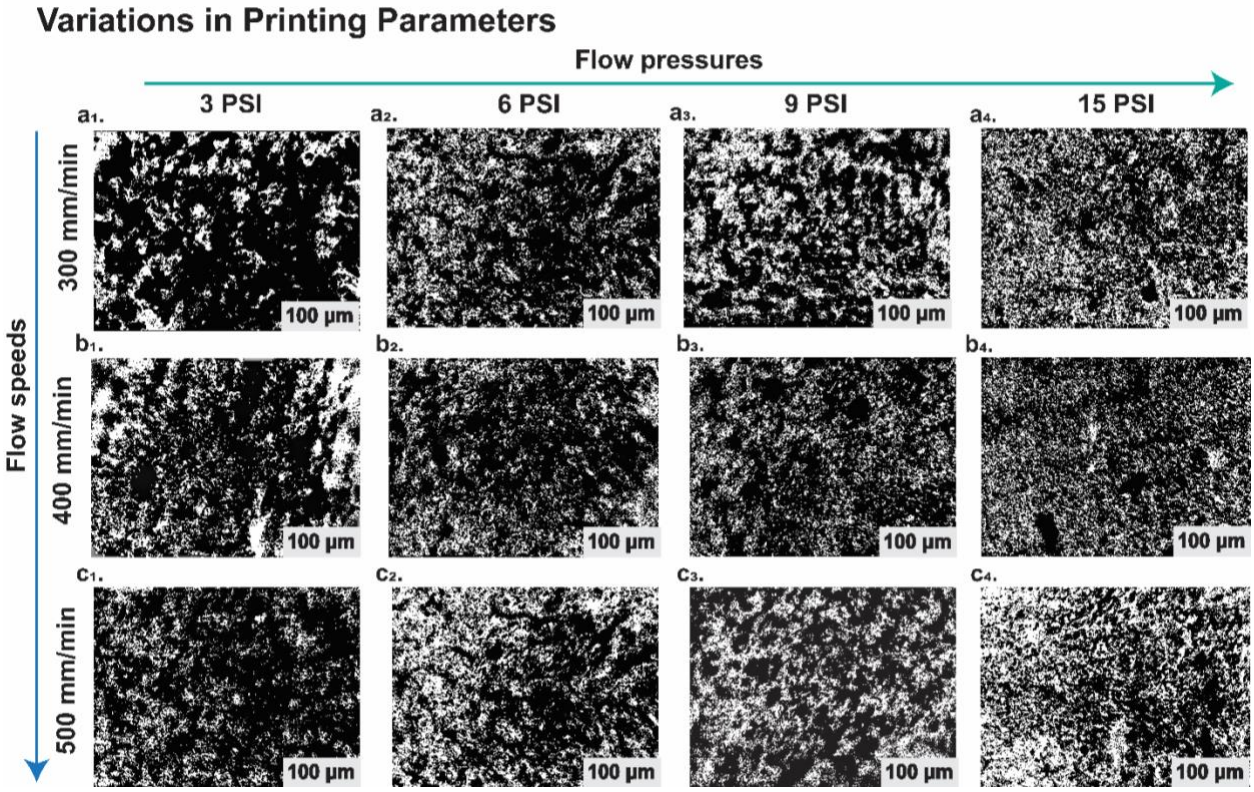

Figure 4. Optical images presented in the figures depict the distribution of Cu filler content within the polymer matrix, where white represents Cu and black signifies the polymer matrix. The images illustrate the impact of different flow pressures, ranging from 3 to 15 PSI on the X-axis, as well as varying flow speeds, spanning from 300 to 500 mm/min on the Y-axis. Each image is accompanied by a 100 µm scale bar for reference (all visualizations were generated using ImageJ software).

By adjusting the printing pressures and speeds, we gained precise control over the flow rate and deposition of the highly viscous inks. This is demonstrated in **Figure 4**, where we quantified the connection pathways observed in the printed film PVDF/PEG/Cu23. The area covered by the filler exhibited variations with different speeds (i.e., 300, 400, and 500 mm/min) and pressures (i.e., 3, 6, 9, and 15 PSI). Notably, pressure variations had a substantial impact on the amount of copper filler deposition. For instance, at an injection speed of 300 mm/min, 3D-printed samples at 3 PSI showed less filler deposition compared to those at 15 PSI under the same injection rate **(Figure 4a$_{1-4}$)**. At higher speeds of 400 mm/min (**Figures 4b$_{1-4}$**) and 500 mm/min (**Figures 4c$_{1-4}$**), respectively, higher pressures resulted in a more uniform Cu distribution and an improved connecting network. Therefore, higher pressure ranges significantly influenced the deposition of filler content, ensuring better deposition alongside the polymer compared to lower pressures.

Moreover, incremental increases in nozzle speed had a notable impact on the extent of aggregation, influencing both the deposition amount and dispersion quality. The investigation into nozzle speed's effect on deposition variations entailed altering the speed across 300 mm/min, 400 mm/min, and 500 mm/min. Under lower pressure conditions (3 psi), raising the injection speed from 300 to 500 mm/min did not significantly reduce the number of clusters, but it did lead to a more uniform Cu distribution within each cluster (as depicted in **Figures $4a_1$-$4c_1$** and **$4a_2$-$4c_2$**, respectively). However, at higher pressure ranges (e.g., 9 and 15 psi), this trend became less apparent. Specifically, the number of clusters and the dispersion quality within each cluster, as seen in **Figure $4a_3$-b_3** or **$4a_4$-b_4**, did not exhibit distinct differences based on the initial imaging analysis.

An initial investigation into the impacts of printing parameters revealed that flow pressure had a more pronounced effect compared to printing speeds. Recognizing the accumulation of Cu particles is crucial for guiding 3D printing; however, relying solely on optical imaging and conventional trial-and-error strategies contradicts the rapid prototyping nature of 3D printing. Additionally, considering other unexamined printing parameters could lead to increased workload, slower material design processes, and more material waste. For instance, our experiments included printing at a pressure of 9 PSI and a speed of around 500 mm/min, with varying concentrations, demonstrating that even a change in concentration resulted in different deposition amounts (see **Figure S6**). Therefore, we explored the feasibility of using real-time monitoring of 3D printing through imaging analysis and machine learning (**section 3.4**) to streamline the decision-making process regarding optimal printing parameters and their effects on composite film properties.

3.3 Machine Learning (ML) for Optimal Printing Parameter Selection

In the realm of 3D printing, making informed decisions regarding printing parameters has posed a considerable challenge in the quest for improved printing quality. The utilization of non-optimal parameter sets often results in wasted printing materials, time, and extensive experimental efforts. Traditionally, domain experts in 3D printing rely on their experience to determine suitable parameters, a process further necessitating trial-and-error experiments for parameter refinement. This decision-making procedure is not only laborious but also time-consuming. To address these challenges, this study proposes the implementation of ML techniques to automate the decision-making process for printing parameters, streamlining the search for optimal parameter values.

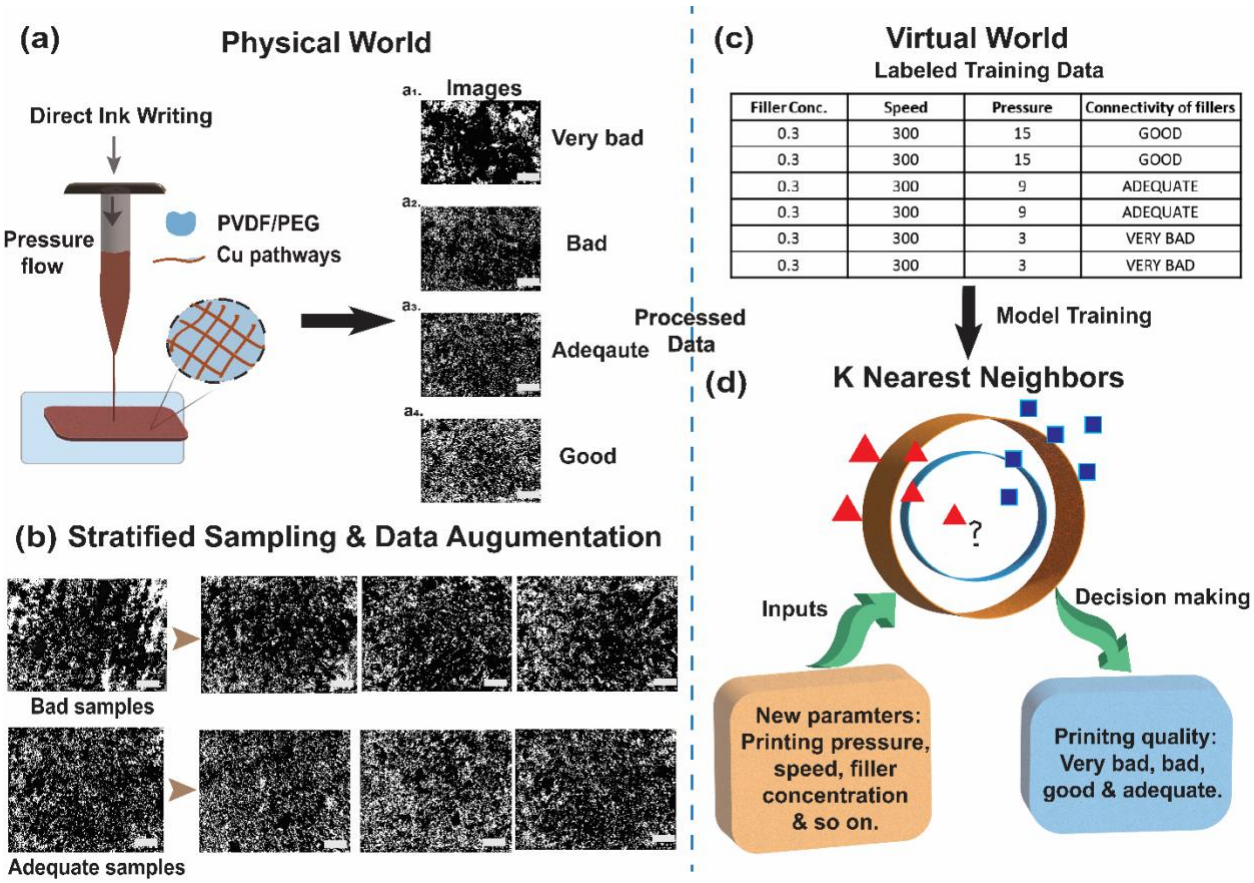

Filler Conc.	Speed	Pressure	Connectivity of fillers
0.3	300	15	GOOD
0.3	300	15	GOOD
0.3	300	9	ADEQUATE
0.3	300	9	ADEQUATE
0.3	300	3	VERY BAD
0.3	300	3	VERY BAD

Figure 5. The parametric study on PVDF20/PEG06/Cu23 printed to film using both expert domain knowledge and machine learning model is presented, highlighting the quality of a) 3D printed sample labeled as a_1) very bad a_2) bad a_3) adequate, and a_4) a good amount of dispersion, for b) stratified sampling and data augmentation for training data construction used as c) training data to validate d) K Nearest Neighbor (KNN) model. Each image is accompanied by a 100 µm scale bar for reference, and all visualizations were generated using ImageJ software. Check **Table S3** for all analysis and labeling.

3.3.1 Data Construction and Augmentation

In this study, several 3D printing experiments were conducted for different parameter sets. We have considered two printing parameters and systematically modulated the printing pressures in between low and high ranges of (3,6,9, 15 PSI) and speeds (300mm/min, 400mm/min & 500mm/min). From **Figure 5a**, a particular concentration which is PVDF/PEG/Cu23 the optical images from **Figures 5a$_1$-5$_4$** the experiments resulted in printed parts, whose quality was evaluated with expert knowledge and labeled as "very bad", "bad", "adequate", and "good". These labels were given to the associated parameter sets, as shown in the table below. Three parameters were considered as the inputs: (1) filler concentrations, (2) printing speeds (3) printing pressures. With their printing quality labels, these parameter sets became the training data for ML models, for rigorous and robust model training and validation, we adopted stratified sampling and data augmentation as shown in **Figure 5b**. This method of sampling involves a population which can be partitioned into subpopulations [44]. For the experimental data, there are 4 classes (subpopulations), i.e., "very bad", "bad", "adequate", and "good". To train and validate KNN models as shown in **Figures 5c-5d**, we partitioned the experimental data into the training and testing sets using stratified sampling. From each class, we drew one data instance, forming a testing set of 4 instances. The rest of the experimental data became training data. Such stratified sampling was done three times. Each time a different instance was drawn from each subpopulation, and the rest instances were kept for training. Eventually, there were 3 different training/testing sets created from the original experimental data. We

employed a pre-trained VGG16 convolutional neural network (CNN) model for feature extraction from raw images[45]. Subsequently, we utilized these features to compute the Euclidean distance between a newly captured image and a reference image [46], enabling us to categorize the newly collected image into one of four labels: good, bad, adequate, or very bad.

The pre-trained VGG16 model extracts features from both the new image and reference images. We then compute the Euclidean distance between the new image's features and those of the reference images, assigning the label of the reference image with the minimum distance as the printing quality label for the new image. This process completes the "data construction" phase, enabling training of our KNN model for printing quality prediction based on given printing parameter sets. In this study, the experimental data size was small, which was insufficient to train the KNN model effectively. Hence, bootstrapping [47] was used to augment the training set's size from 17 instances to 100 instances. Specifically, 100 uniforms [0, 1] random numbers $z_1, z_2 \dots, z_{100}$, were generated and rounded to aa floorseige in x as $i = \lfloor z_i \cdot 17 \rfloor + 1, i = 1, 2, \dots, 0$. The indices were used to bootstrap samples from the initial 17 training instances with replacement. (Note that the testing data were not part of the bootstrapping and were not used for model training in any sense.)

3.3.2 Printing Quality Prediction with Trained K-Nearest Neighbors (KNN)

K-Nearest Neighbors (KNN) is a non-parametric supervised ML method that can be used for classification or regression [48].It relies on distance for classification. The output is class membership. If K=1, then the instance is simply assigned to the class of that single nearest neighbor. This study adopted KNN, with K=3, to classify (predict) the printing quality based on the input printing parameters as shown in **Table 2**.

Table 2. Testing data and prediction performance using input printing parameters.

Testing Set-1	**Filler Conc. (wt%)**	**Speed (mm/min)**	**Pressure (PSI)**	**Connectivity Labeling**
0	*23*	*300*	*15*	*GOOD*
1		*300*	*9*	*ADEQUATE*
2		*300*	*6*	*BAD*
3		*300*	*3*	*VERY BAD*
Testing Set-2	**Filler Conc.**	**Speed**	**Pressure**	**Connectivity**
0	*23*	*300*	*15*	*GOOD*
1		*400*	*6*	*ADEQUATE*
2		*500*	*6*	*BAD*
3		*400*	*3*	*VERY BAD*
Testing Set-3	**Filler Conc.**	**Speed**	**Pressure**	**Connectivity**
0	*23*	*400*	*15*	*GOOD*
1		*300*	*9*	*ADEQUATE*
2		*500*	*3*	*VERY BAD*
3		*300*	*6*	*BAD*

We have taken the above input parameters for testing data of the sample and generated into confusion matrices to understand the prediction performance of the KNN model, we have given two more identical matrices as shown in **Table 3.** The predicted performance for the three KNN models was all 100%. Perfect accuracy implies that one can use these KNN models to predict the printing quality for new parameter sets with high confidence. In accounting for this prediction, we were able to further our testing based on the optimized printing parameter. This resulted in minimizing the trial-and-error process for selecting the printing parameters to assess the low percolation threshold parameter showing better performance, we have used the ML model to train the data sets. ML allows anomaly detection through a large dataset of good

printing samples and bad printing samples and the detection capability can be improved by adding new training data. Based on the given parameter from ML, the optimized parameter to use to attain a good conductivity network, this has been implemented and printed further films and tested to see the performance of the films.

Table 3. Highlights a matrix of actual (**Figure 4**) and predicted results of the labeled parameters (**Table 2**)

Actual/Predicted	Very bad	Bad	Adequate	Good
Very bad	1	0	0	0
Bad	0	1	0	0
Adequate	0	0	1	0
Good	0	0	0	1

3.4 Electrical and Mechanical Performance Properties of 3D Printed CPC Film

Utilizing the ML-optimized printing parameter dataset, which included printing speed and pressure settings, we conducted 3D printing experiments to explore the structure-property relationships of these composites. Our primary focus was on understanding the impact of copper concentrations (ranging from 8% to 54% by weight) on the electrical conductivity of the CPCs, particularly in relation to conducting pathways within the composites, interparticle distances, and Cu dispersion quality. The anisotropy of copper dendrites within conductive films has been a subject, as their orientation influenced by both their morphology and the printing technique employed, significantly impacts the electrical conductivity of the material. Studies indicate that when dendrites are aligned in a specific direction, it can result in varying conductivity levels along different axes of the film due to the directional nature of the dendritic structures. For instance, the electrical properties of films are influenced by the orientation of these dendrites, which in turn is controlled by the directionality of the printing process [49,50]. This is why electrical measurements are typically conducted in the through-plane direction, consistent with the orientation in which the films are printed. The rationale is to assess the conductivity in a manner that aligns with the natural flow of charge, which is intrinsically linked to the orientation of the composite particles as they are laid down during the printing process. The findings from such assessments provide insights into optimizing the printing strategies for conductive films to achieve desired electrical performance characteristics.

As depicted in **Figure 6a**, the trend in conductivity measurements with respect to copper concentrations revealed a gradual increase, reaching approximately 0.2 S/cm when the Cu content reached 54 wt.%. This explains that the combination of binary blend matrix has high insulating properties and extremely low electrical conductivities, for instance, PVDF has a low electrical conductivity of around 10^{-11} S/cm, resulting in a high percolation threshold of Cu. Moreover, the oxidation of Cu will also impact the electrical conductivity range which can be improved by coatings, or the addition of other fillers and so on [7,22]. From the curve fitting, we can understand that above 23 wt.%, the Cu has its cluster formation which enhances the electrical conductivity. The percolation transition occurs as the conducting concentration approaches the percolation threshold, and the condition transitions from non-ohmic to ohmic. The percolation threshold of the copper content is calculated using the power law scaling law defined by **Equation 1**.

$$\sigma = \sigma_0(P-P_c)^t \qquad \textit{Equation 1}$$

where σ_0 is the scaling factor, P is the conductive volume factor, P_c is the conductive volume fraction for the electrical percolation threshold, and t is the conductivity exponent [41,42].

Furthermore, we investigated the thermo-resistive behavior of these CPC films at elevated temperatures, reaching up to 160°C, to examine their switching characteristics and stability under extreme conditions. **Figure 6b** provides insights into the temperature-dependent conductivity of the PVDF/PEG/Cu films. As the temperature increases, the resistivity of the films also rises, indicating a decrease in conductivity due to reduced effective connections within the copper conductive layer. This behavior is of paramount importance in preventing thermal runaway or overheating, particularly in battery applications. For instance,

in the case of PVDF/PEG/Cu54, with the highest copper content, the resistance at room temperature is approximately 20 ohms. However, as the temperature gradually climbs to around 100°C, this resistance dramatically surges to approximately 10^8 mega-ohms. The resistivity experiences an increase of about 8 orders of magnitude as the temperature elevates from 30 to 100°C. This results in a resistivity change rate of approximately $4 \times 10^7\ \Omega\,\text{cm}/^{o}\text{C}$ at the range of 90–100 °C. Consequently, the film demonstrates remarkable stability up to a maximum temperature of 160°C, beyond which it automatically shuts down without exhibiting NTC behavior. This wide temperature range renders the film suitable for use as a heat protector in various applications. Notably, the reported resistivity change and the encompassed temperature range are significantly higher, approximately 10^2–10^3 times greater, than those observed in previous PTC composites employed in lithium-ion batteries (LIBs), such as poly(methyl methacrylate) (PMMA)/carbon black (CB) [13,51] and polyethylene (PE)/carbon black (CB) [52].

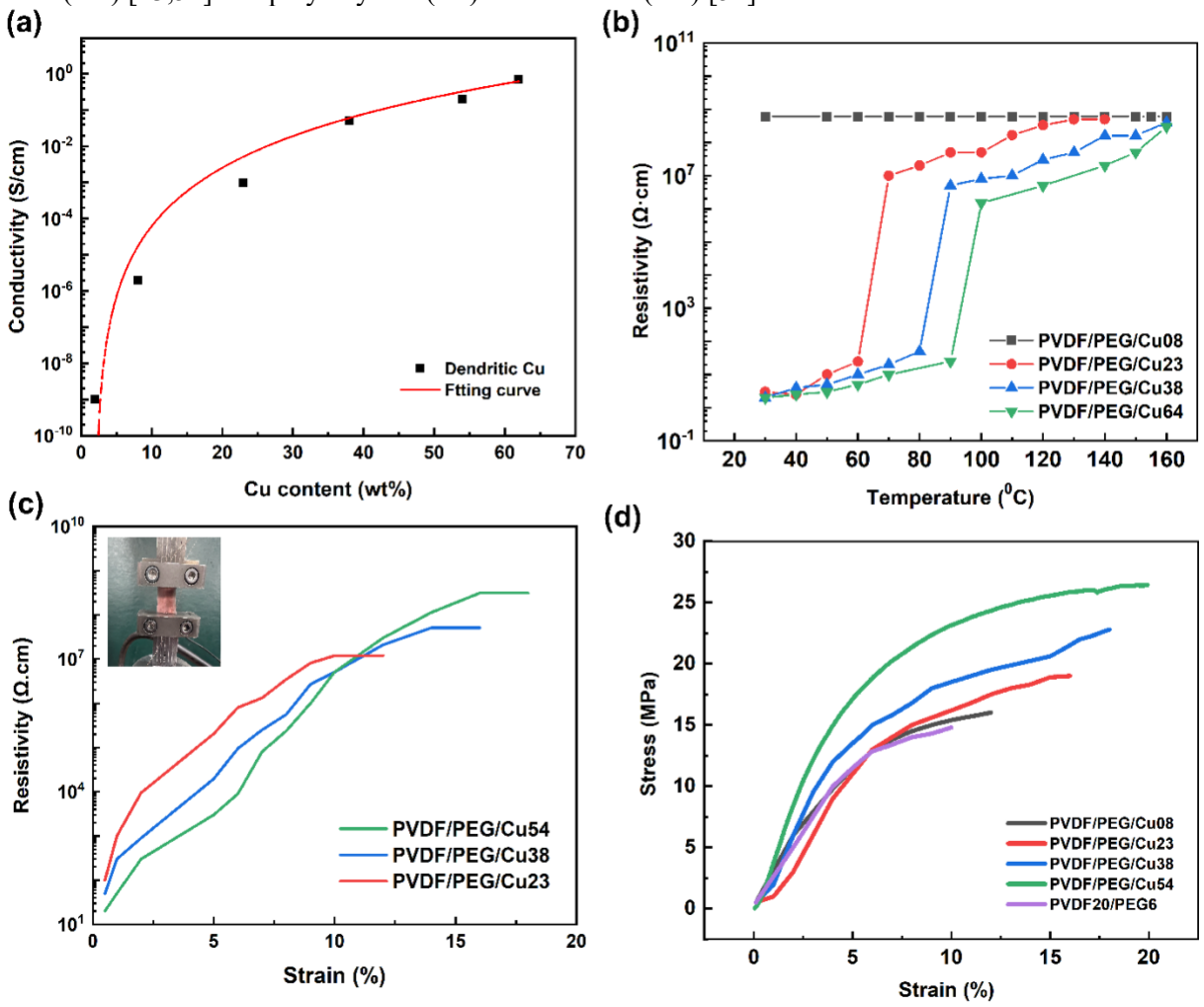

Figure 6. The electrical characteristics of composite films were examined through several aspects: a) assessing the electrical conductivity as a function of the weight fraction of Cu, where the curve represents the best-fit line for conductivity above the percolation threshold as per percolation theory, revealing a non-linear increase in conductivity with varying Cu weight percentages; b) analyzing the alteration in resistivity with temperature; c) exploring the change in resistivity as a function of strain; and d) examining the stress vs. strain curves obtained from mechanical tension tests.

This behavior is consistent with the typical response of most materials (e.g. semi-conducting materials), where higher temperatures lead to increased electron scattering and, consequently, greater electrical resistance. However, it is crucial to examine how these trends evolve and their impact. One attractive feature

of this approach is that the switching temperature can be rationally designed to meet the requirement of the operating temperature by adjusting its composition. For instance, the switching temperature decreased to approximately 60 and 80 °C for PVDF/PEG with 23 and 38 wt% of Cu, respectively. Accordingly, we can tune the behavior with deposition control depending on the application. The intricate balance between copper concentration and temperature significantly influences the connectivity of conductive pathways within the PVDF/PEG/Cu films (**Figure S7**). This mechanism unfolds as follows: just above the melting point of PEG, the resistance starts to increase, indicating the initiation of a phase change in the polymer matrix. The expansion of PEG causes a reduction in the distance between filler particles in the PVDF phase, leading to increased particle interaction. Consequently, more energy is required to break these interactions, resulting in an intensified Positive Temperature Coefficient effect [52]. As the temperature continues to rise, the influence of higher copper concentrations becomes more pronounced. The denser distribution of copper particles within the material disrupts the formation of continuous conductive pathways in the PVDF phase due to high interfacial energies [17,53]. This suggests that a greater concentration of copper may exacerbate the material's conductivity at elevated temperatures. In the case of a temperature spike or thermal runaway, this could impact the material's ability to efficiently disperse heat. However, when copper content exceeds the percolation threshold, the films become highly efficient at conducting current, especially at elevated temperatures. This behavior has significant implications for thermal shutdown mechanisms, particularly in applications where effective heat dissipation and control are crucial for thermal management [54,55].

Our study also delved into the strain-sensing capabilities of these CPCs, as illustrated in **Figure 6c**. Despite initial variations from different filler content concentrations, a consistent trend emerged, indicating a logarithmic increase in resistivity with strain for all samples. Notably, even minor changes in filler content led to noticeable adjustments in the resistivity-strain slope coefficient. Lowering the filler content resulted in enhanced sensitivity, prompting tests to be conducted on films with higher copper concentrations than PVDF/PEG/Cu08. The figure demonstrates that PVDF/PEG/Cu54 exhibits a gradual increase in resistivity with an increase in strain, reaching approximately 20%, in line with the observations in **Figure 6d**. Beyond a strain of 20%, the films function as insulators, completely interrupting the flow of current. This behavior can be attributed to improved network connectivity achieved through the optimization of printing parameters using ML. Additionally, it's worth mentioning that future research may investigate the percolation threshold of filler content with binary fillers to avoid oxidation of metallic fillers concerning various particle shapes and sizes, as the formation of 2D or 3D filler particle networks can vary significantly[56].

The previously mentioned mechanism also exerts a significant influence on the mechanical properties of the films, which were assessed through mechanical tension tests (**Figure 6d**). These tests were conducted to gain valuable insights into the film's mechanical properties (**Table 4**). The stress vs. strain testing method was employed, with the strain percentage carefully controlled to observe the impact of filler particles on the modulus while maintaining a consistent strain rate. This approach allowed us to investigate how properties were affected before a comprehensive disruption in the filler network within the film. It is worth highlighting that good adhesion and network structure can increase the modulus with filler concentration, although there is a saturation limit. As shown in **Figure 6d**, the inclusion of fillers enhances the interfacial bonding between the polymer matrix and the filler material. The modulus of PVDF/PEG increased from 471±1.70 MPa to 481±1.54 MPa (**Table 4**), with a similar trend of strength and strain before the composites became insulating. This noticeable increase supports the crucial role of enhanced adhesion in facilitating stress transfer between different phases, ultimately resulting in improved modulus, strength, and even toughness properties. Similar observations have been made in previous studies, where the reinforcing effect of metal fillers has been shown to impact mechanical properties significantly.

Table 4. Correlation of polymer concentrations with their mechanical properties

Polymer Composite Blend	Modulus (MPa)	Strength (MPa) at conductivity cutoff	Strain (%) at conductivity cutoff
PVDF20/PEG06	*473.01±1.70*	*14.05±0.25*	*10.04±0.16*
PVDF/PEG/Cu08	*477.30±3.41*	*16.12±0.32*	*12.53±0.10*
PVDF/PEG/Cu23	*475.12±2.12*	*19.03±0.12*	*15.31±0.13*
PVDF/PEG/Cu38	*476.31±0.80*	*23.20±0.24*	*17.12±0.17*
PVDF/PEG/Cu54	*481.10±1.54*	*26.02±0.19*	*20.13±0.09*

4. Conclusion

In summary, our study presents an innovative approach that combines DIW with ML-assisted quality control to optimize the fabrication of conductive polymer composites. Our main objective was to finely tune the printing parameters to strike a balance between maximizing particle connectivity (e.g., higher copper loading and connectivity) and ensuring uniform distributions (e.g., electrical conductivity and mechanical durability). This novel approach significantly enhances the rapid prototyping of 3D printed composites, eliminating the need for time-consuming practices through aided model training, particularly with the KNN model. Furthermore, by implementing stratified sampling, data augmentation, and bootstrapping techniques, we expanded our training dataset from 17 instances to 100 instances, thus improving our model's predictive capabilities. Through meticulous control of printing variables such as flow speed, pressure, and filler concentration, we have achieved remarkable results. Our CPC films exhibit a wide operating temperature range from 30 to 160°C, with an electrical conductivity of approximately 0.2 S/cm. Additionally, these films display increased modulus and strain-sensing capabilities with higher filler content. These findings hold significant promise for the development and customization of highly functional thermal interface materials applicable in sensors, current collectors, and various energy storage devices.

5. Declaration of competing interest

The authors declare the following financial interests/personal relationships which may be considered as potential competing interests:

6. Acknowledgment

We appreciate the funding from the NSF CAREER (award # 2145895), AFOSR (award # FA9550-22-1-0263), ACS PRF (award # 62371-ND10), and U.S. National Science Foundation EFRI (award # 2132183).

7. References

[1] Z. Wang, Z. Wu, L. Weng, S. Ge, D. Jiang, M. Huang, D.M. Mulvihill, Q. Chen, Z. Guo, A. Jazzar, X. He, X. Zhang, B. Bin Xu, A Roadmap Review of Thermally Conductive Polymer Composites: Critical Factors, Progress, and Prospects, Adv Funct Mater 33 (2023) 2301549. https://doi.org/10.1002/ADFM.202301549.

[2] X. Xu, J. Chen, J. Zhou, B.X. Li F Xu, J. Chen, J. Zhou, X.F. Xu, B.W. Li, Thermal Conductivity of Polymers and Their Nanocomposites, Advanced Materials 30 (2018) 1705544. https://doi.org/10.1002/ADMA.201705544.

[3] W. Yu, C. Liu, L. Qiu, P. Zhang, W. Ma, Y. Yue, H. Xie, L.A. Sarah Larkin, Advanced thermal interface materials for thermal management, Engineered Science 2 (2018) 1–3. https://doi.org/10.30919/ES8D710.

[4] J. Chen, Y. Zhu, J. Huang, J. Zhang, D. Pan, J. Zhou, J.E. Ryu, A. Umar, Z. Guo, Advances in Responsively Conductive Polymer Composites and Sensing Applications, Polymer Reviews 61 (2021) 157–193. https://doi.org/10.1080/15583724.2020.1734818.

[5] H. Liu, Q. Li, S. Zhang, R. Yin, X. Liu, Y. He, K. Dai, C. Shan, J. Guo, C. Liu, C. Shen, X. Wang, N. Wang, Z. Wang, R. Wei, Z. Guo, Electrically conductive polymer composites for smart flexible strain sensors: a critical review, J Mater Chem C Mater 6 (2018) 12121–12141. https://doi.org/10.1039/C8TC04079F.

[6] J. Allen, Review of polymers in the prevention of thermal runaway in lithium-ion batteries, in: Energy Reports, Elsevier Ltd, 2020: pp. 217–224. https://doi.org/10.1016/j.egyr.2020.03.027.

[7] S. Baranek, V. Cerny, R. Drochytka, L. Meszarosova, J. Melichar, Electrically conductive composite materials with incorporated waste and secondary raw materials, Scientific Reports 2023 13:1 13 (2023) 1–23. https://doi.org/10.1038/s41598-023-36287-x.

[8] S.A. Hosseini Pour, B. Pourabbas, M. Salami Hosseini, Electrical and rheological properties of PMMA/LDPE blends filled with carbon black, Mater Chem Phys 143 (2014) 830–837. https://doi.org/10.1016/J.MATCHEMPHYS.2013.10.021.

[9] H. Ma, S. Zong, B. Wan, G. Wang, Q. Tian, Application of power battery under thermal conductive silica gel plate in new energy vehicles, Scientific Reports 2024 14:1 14 (2024) 1–14. https://doi.org/10.1038/s41598-023-43388-0.

[10] Q. Wang, P. Ping, X. Zhao, G. Chu, J. Sun, C. Chen, Thermal runaway caused fire and explosion of lithium ion battery, J Power Sources 208 (2012) 210–224. https://doi.org/10.1016/J.JPOWSOUR.2012.02.038.

[11] S. Ma, M. Jiang, P. Tao, C. Song, J. Wu, J. Wang, T. Deng, W. Shang, Temperature effect and thermal impact in lithium-ion batteries: A review, Progress in Natural Science: Materials International 28 (2018) 653–666. https://doi.org/10.1016/J.PNSC.2018.11.002.

[12] R. Zhang, P. Tang, J. Li, D. Xu, Y. Bin, Study on filler content dependence of the onset of positive temperature coefficient (PTC) effect of electrical resistivity for UHMWPE/LDPE/CF composites based on their DC and AC electrical behaviors, Polymer (Guildf) 55 (2014) 2103–2112. https://doi.org/10.1016/J.POLYMER.2014.02.065.

[13] Q. Zhang, J. Wang, B.H. Guo, Z.X. Guo, J. Yu, Electrical conductivity of carbon nanotube-filled miscible poly(phenylene oxide)/polystyrene blends prepared by melt compounding, Compos B Eng 176 (2019) 107213. https://doi.org/10.1016/J.COMPOSITESB.2019.107213.

[14] L. Xia, L.M. Zhu, H.Y. Zhang, X.P. Ai, A positive-temperature-coefficient electrode with thermal protection mechanism for rechargeable lithium batteries, Chinese Science Bulletin 57 (2012) 4205–4209. https://doi.org/10.1007/S11434-012-5071-9.

[15] X. Zhang, S. Zheng, H. Zou, X. Zheng, Z. Liu, W. Yang, M. Yang, Two-step positive temperature coefficient effect with favorable reproducibility achieved by specific "island-bridge" electrical conductive networks in HDPE/PVDF/CNF composite, Compos Part A Appl Sci Manuf 94 (2017) 21–31. https://doi.org/10.1016/J.COMPOSITESA.2016.12.001.

[16] C.P. Feng, L.Y. Yang, J. Yang, L. Bai, R.Y. Bao, Z.Y. Liu, M.B. Yang, H.B. Lan, W. Yang, Recent advances in polymer-based thermal interface materials for thermal management: A mini-review, Composites Communications 22 (2020) 100528. https://doi.org/10.1016/J.COCO.2020.100528.

[17] Y. Wei, Z. Li, X. Liu, K. Dai, G. Zheng, C. Liu, J. Chen, C. Shen, Temperature-resistivity characteristics of a segregated conductive CB/PP/UHMWPE composite, Colloid Polym Sci 292 (2014) 2891–2898. https://doi.org/10.1007/S00396-014-3334-5.

[18] Q. Li, Siddaramaiah, N.H. Kim, G.H. Yoo, J.H. Lee, Positive temperature coefficient characteristic and structure of graphite nanofibers reinforced high density polyethylene/carbon black nanocomposites, Compos B Eng 40 (2009) 218–224. https://doi.org/10.1016/J.COMPOSITESB.2008.11.002.

[19] D. Ravichandran, M. Kakarla, W. Xu, S. Jambhulkar, Y. Zhu, M. Bawareth, N. Fonseca, D. Patil, K. Song, 3D-printed in-line and out-of-plane layers with stimuli-responsive intelligence, Compos B Eng 247 (2022) 110352. https://doi.org/10.1016/J.COMPOSITESB.2022.110352.

[20] N. Fonseca, S.V. Thummalapalli, S. Jambhulkar, D. Ravichandran, Y. Zhu, D. Patil, V. Thippanna, A. Ramanathan, W. Xu, S. Guo, H. Ko, M. Fagade, A.M. Kannan, Q. Nian, A. Asadi, G. Miquelard-Garnier, A. Dmochowska, M.K. Hassan, M. Al-Ejji, H.M. El-Dessouky, F. Stan, K. Song, 3D Printing-Enabled Design and Manufacturing Strategies for Batteries: A Review, Small 19 (2023) 2302718. https://doi.org/10.1002/SMLL.202302718.

[21] G.J.H. Lim, Z. Lyu, X. Zhang, J.J. Koh, Y. Zhang, C. He, S. Adams, J. Wang, J. Ding, Robust pure copper framework by extrusion 3D printing for advanced lithium metal anodes, J Mater Chem A Mater 8 (2020) 9058–9067. https://doi.org/10.1039/D0TA00209G.

[22] L.F. Figueiredo, F.S. Vieira, O.D. Jamieson, J. Reeder, T. Mc Lean, J. Olsen, R.D. Crapnell, M.J. Whittingham, C.E. Banks, R. Law, J. Gruber, M. Peeters, Influence of design and material characteristics on 3D printed flow-cells for heat transfer-based analytical devices, Microchimica Acta 189 (2022) 1–12. https://doi.org/10.1007/S00604-022-05163-2.

[23] M. Rana, M. Bhushan, Machine learning and deep learning approach for medical image analysis: diagnosis to detection, Multimed Tools Appl 82 (2023) 26731–26769. https://doi.org/10.1007/S11042-022-14305-W.

[24] S. Ferdousi, R. Advincula, A.P. Sokolov, W. Choi, Y. Jiang, Investigation of 3D printed lightweight hybrid composites via theoretical modeling and machine learning, Compos B Eng 265 (2023) 110958. https://doi.org/10.1016/J.COMPOSITESB.2023.110958.

[25] D.J. Roach, A. Rohskopf, C.M. Hamel, W.D. Reinholtz, R. Bernstein, H.J. Qi, A.W. Cook, Utilizing computer vision and artificial intelligence algorithms to predict and design the mechanical compression response of direct ink write 3D printed foam replacement structures, Addit Manuf 41 (2021) 101950. https://doi.org/10.1016/J.ADDMA.2021.101950.

[26] Y. Zhu, T. Kwok, J.C. Haug, S. Guo, X. Chen, W. Xu, D. Ravichandran, Y.D. Tchoukalova, J.L. Cornella, J. Yi, O. Shefi, B.L. Vernon, D.G. Lott, J.N. Lancaster, K. Song, 3D Printable Hydrogel with Tunable Degradability and Mechanical Properties as a Tissue Scaffold for Pelvic Organ Prolapse Treatment, Adv Mater Technol 8 (2023). https://doi.org/10.1002/ADMT.202201421.

[27] C. Janiesch, P. Zschech, K. Heinrich, Machine learning and deep learning, Electronic Markets 31 (2021) 685–695. https://doi.org/10.1007/S12525-021-00475-2.

[28] S. Rashid, M. Raza, M. Sharif, F. Azam, S. Kadry, J. Kim, White blood cell image analysis for infection detection based on virtual hexagonal trellis (VHT) by using deep learning, Sci Rep 13 (2023). https://doi.org/10.1038/s41598-023-44352-8.

[29] W. Xu, S. Jambhulkar, Y. Zhu, D. Ravichandran, M. Kakarla, B. Vernon, D.G. Lott, J.L. Cornella, O. Shefi, G. Miquelard-Garnier, Y. Yang, K. Song, 3D printing for polymer/particle-based processing: A review, Compos B Eng 223 (2021) 109102. https://doi.org/10.1016/J.COMPOSITESB.2021.109102.

[30] D. Ravichandran, W. Xu, M. Kakarla, S. Jambhulkar, Y. Zhu, K. Song, Multiphase direct ink writing (MDIW) for multilayered polymer/nanoparticle composites, Addit Manuf 47 (2021). https://doi.org/10.1016/J.ADDMA.2021.102322.

[31] H. Zhao, Y. Fu, M. Ling, Z. Jia, X. Song, Z. Chen, J. Lu, K. Amine, G. Liu, Conductive Polymer Binder-Enabled SiO-SnxCoyCz Anode for High-Energy Lithium-Ion Batteries, ACS Appl Mater Interfaces 8 (2016) 13373–13377. https://doi.org/10.1021/ACSAMI.6B00312.

[32] K. Lee, S. Lim, T.H. Kim, Dopamine-conjugated Poly(acrylic acid) Blended with an Electrically Conductive Polyaniline Binder for Silicon Anode, Bull Korean Chem Soc 39 (2018) 873–878. https://doi.org/10.1002/BKCS.11492.

[33] L. Lin, S. Liu, Q. Zhang, X. Li, M. Ji, H. Deng, Q. Fu, Towards tunable sensitivity of electrical property to strain for conductive polymer composites based on thermoplastic elastomer, ACS Appl Mater Interfaces 5 (2013) 5815–5824. https://doi.org/10.1021/AM401402X.

[34] J. Gonzalez-Gutierrez, G.B. Stringari, Z.M. Megen, al -, P. Bhattacharya, J. Kumar, M.I. Nandasiri, Review—Conducting Polymer-Based Binders for Lithium-Ion Batteries and

Beyond, J Electrochem Soc 167 (2020) 065501. https://doi.org/10.1149/1945-7111/AB856B.

[35] R. Huang, J. Xie, X. Wu, G. Zhang, X. Yang, Preparation of Composite Cooling Boards Composed of Thermal Conductive Silica Gel and Phase Change Materials for Battery Thermal Management, Energy and Fuels 35 (2021) 13466–13473. https://doi.org/10.1021/ACS.ENERGYFUELS.1C01966.

[36] X. Yang, J. Liu, N. Pei, Z. Chen, R. Li, L. Fu, P. Zhang, J. Zhao, The Critical Role of Fillers in Composite Polymer Electrolytes for Lithium Battery, Nano-Micro Letters 2023 15:1 15 (2023) 1–37. https://doi.org/10.1007/S40820-023-01051-3.

[37] Y.P. Mamunya, H. Zois, L. Apekis, E. V. Lebedev, Influence of pressure on the electrical conductivity of metal powders used as fillers in polymer composites, Powder Technol 140 (2004) 49–55. https://doi.org/10.1016/J.POWTEC.2003.11.010.

[38] Z. Chen, P.C. Hsu, J. Lopez, Y. Li, J.W.F. To, N. Liu, C. Wang, S.C. Andrews, J. Liu, Y. Cui, Z. Bao, Fast and reversible thermoresponsive polymer switching materials for safer batteries, Nat Energy 1 (2016). https://doi.org/10.1038/nenergy.2015.9.

[39] H. Guo, T. Xu, S. Zhou, F. Jiang, L. Jin, N. Song, P. Ding, A technique engineered for improving thermal conductive properties of polyamide-6 composites via hydroxylated boron nitride masterbatch-based melt blending, Compos B Eng 212 (2021) 108716. https://doi.org/10.1016/J.COMPOSITESB.2021.108716.

[40] Y.C. Sun, M. Chu, M. Huang, O. Hegazi, H.E. Naguib, Hybrid Electroactive Shape Memory Polymer Composites with Room Temperature Deformability, Macromol Mater Eng 304 (2019) 1900196. https://doi.org/10.1002/MAME.201900196.

[41] G. Raos, B. Zappone, Polymer Adhesion: Seeking New Solutions for an Old Problem #, Macromolecules 54 (2021) 10617–10644. https://doi.org/10.1021/ACS.MACROMOL.1C01182.

[42] W. Xu, S. Jambhulkar, Y. Zhu, D. Ravichandran, M. Kakarla, B. Vernon, D.G. Lott, J.L. Cornella, O. Shefi, G. Miquelard-Garnier, Y. Yang, K. Song, 3D printing for polymer/particle-based processing: A review, Compos B Eng 223 (2021) 109102. https://doi.org/10.1016/J.COMPOSITESB.2021.109102.

[43] S. Jambhulkar, W. Xu, R. Franklin, D. Ravichandran, Y. Zhu, K. Song, Integrating 3D printing and self-assembly for layered polymer/nanoparticle microstructures as high-performance sensors, J Mater Chem C Mater 8 (2020) 9495–9501. https://doi.org/10.1039/D0TC02660C.

[44] H. Sahu, W. Rao, A. Troisi, H. Ma, Toward Predicting Efficiency of Organic Solar Cells via Machine Learning and Improved Descriptors, Adv Energy Mater 8 (2018) 1801032. https://doi.org/10.1002/AENM.201801032.

[45] Abdullah, M.S. Hasan, An application of pre-trained CNN for image classification, International Conference on Communications and Information Technology 2018-January (2017) 1–6. https://doi.org/10.1109/ICCITECHN.2017.8281779.

[46] L. Wang, Y. Zhang, J. Feng, On the Euclidean Distance of Images, IEEE Trans Pattern Anal Mach Intell 27 (2005) 1334–1339. https://doi.org/10.1109/TPAMI.2005.165.

[47] R.Y. Rubinstein, Simulation and the Monte Carlo Method, (1981). https://doi.org/10.1002/9780470316511.

[48] T.M. Cover, P.E. Hart, Nearest neighbor pattern classification, IEEE Trans Inf Theory 13 (1967) 21–27. https://doi.org/10.1109/TIT.1967.1053964.

[49] S. Park, W. Shou, L. Makatura, W. Matusik, K. (Kelvin) Fu, 3D printing of polymer composites: Materials, processes, and applications, Matter 5 (2022) 43–76. https://doi.org/10.1016/J.MATT.2021.10.018.

[50] C. V. Manzano, B. Abad, M. Muñoz Rojo, Y.R. Koh, S.L. Hodson, A.M. Lopez Martinez, X. Xu, A. Shakouri, T.D. Sands, T. Borca-Tasciuc, M. Martin-Gonzalez, Anisotropic Effects on the Thermoelectric Properties of Highly Oriented Electrodeposited Bi2Te3 Films, Scientific Reports 2016 6:1 6 (2016) 1–8. https://doi.org/10.1038/srep19129.

[51] M.H. Al-Saleh, U. Sundararaj, Electrically conductive carbon nanofiber/polyethylene composite: effect of melt mixing conditions, Polym Adv Technol 22 (2011) 246–253. https://doi.org/10.1002/PAT.1526.

[52] W. Dafu, Z. Tiejun, X.-S. Yi, Resistivity-Volume Expansion Characteristics of Carbon Black-Loaded Polyethylene, J Appl Polym Sci 77 (2000) 53–58. https://doi.org/10.1002/(SICI)1097-4628(20000705)77:1.

[53] D. Wang, H. Wei, Y. Lin, P. Jiang, H. Bao, X. Huang, Achieving ultrahigh thermal conductivity in Ag/MXene/epoxy nanocomposites via filler-filler interface engineering, Compos Sci Technol 213 (2021) 108953. https://doi.org/10.1016/J.COMPSCITECH.2021.108953.

[54] V.I. Roldughin, V. V. Vysotskii, Percolation properties of metal-filled polymer films, structure and mechanisms of conductivity, Prog Org Coat 39 (2000) 81–100. https://doi.org/10.1016/S0300-9440(00)00140-5.

[55] A. Boudenne, L. Ibos, M. Fois, J.C. Majesté, E. Géhin, Electrical and thermal behavior of polypropylene filled with copper particles, Compos Part A Appl Sci Manuf 36 (2005) 1545–1554. https://doi.org/10.1016/J.COMPOSITESA.2005.02.005.

[56] S. Yu, J.W. Lee, T.H. Han, C. Park, Y. Kwon, S.M. Hong, C.M. Koo, Copper shell networks in polymer composites for efficient thermal conduction, ACS Appl Mater Interfaces 5 (2013) 11618–11622. https://doi.org/10.1021/AM4030406.